



Contents lists available at ScienceDirect

# Mechanical Systems and Signal Processing

journal homepage: [www.elsevier.com/locate/ymssp](http://www.elsevier.com/locate/ymssp)



## Nonlinear study on a rigid rotor supported by herringbone grooved gas bearings: Theory and validation

Wanhui Liu <sup>\*</sup>, Philipp Bättig, Patrick H. Wagner, Jürg Schiffmann

Department of Mechanical Engineering, Laboratory for Applied Mechanical Design, Ecole Polytechnique Fédérale de Lausanne, CH-2000 Neuchâtel, Switzerland



### ARTICLE INFO

#### Article history:

Received 10 December 2019

Received in revised form 7 May 2020

Accepted 13 May 2020

Available online 30 May 2020

#### Keywords:

Gas bearing

Herringbone

Rotordynamics

### ABSTRACT

The nonlinear behavior of a rigid rotor supported by herringbone grooved journal gas bearings (HGJBs) was investigated in this study. The two-dimensional narrow groove theory (2D-NGT) was adopted to model the HGJBs. A set of integrated rotor-bearing state equations were built by coupling the rotor motion equations and the bearing Reynolds equation. An implicit integrator with adaptive time step method was used to solve those state equations continuously. Two low-stability HGJBs were implemented to experimentally demonstrate and analyze the appearance of self-excitation motions. The theoretical model was successfully validated by the experimental data on predicting the onset speed of the sub-synchronous vibration of the HGJB-rotor system and the whirl frequency ratio. The predicted limit cycle amplitude increases as the speed increases until the rotor contacts with the bearing surface, which leads to a bearing failure. Forward conical mode dominates the self-excited motion during the whole speed range of self-excited motion. The prediction shows that the HGJB-rotor system can still operate in a stable, even though the rotor is installed vertically, i.e., without static load on the bearings. This is a distinct advantage in comparison to plain bearings. As the static load applies on the bearings increases, the onset speed of sub-synchronous vibration increases as well. For the investigated rotor-bearing system, an increase of the onset speed of sub-synchronous vibration from 36 krpm to 75 krpm is predicted as the static load increases from 0 to 4 times of the rotor weight. This indicates an increased HGJB stability with increased static load. The rotor orbits show complex shapes when the imbalance excitation is considered in the simulation. Both synchronous frequency and whirl frequency are shown in the spectral analysis. Moreover, the speed range of self-excited motion reduces from [38,48] krpm to [40,42] krpm as the imbalance increases from 0 to 40 mgmm.

© 2020 Elsevier Ltd. All rights reserved.

### 1. Introduction

Gas lubricated bearings are widely used in high-speed rotating machinery, e.g., gyroscopes [1], turbo compressors [2], turbo blowers [3], micro gas turbines [4,5], turbochargers [6], and air cycle machines for aircrafts [7] due to their distinct advantages such as oil-free, low friction, compact structure, and extreme temperature resilience [8,9]. The herringbone grooved journal bearing (HGJB) is a promising self-acting rigid surface gas bearing design. Besides the advantages listed above, this type of bearing can operate with radial clearance of several micrometers, which is beneficial for small-scale

\* Corresponding author.

E-mail addresses: [wanhui.liu@epfl.ch](mailto:wanhui.liu@epfl.ch) (W. Liu), [philipp.battig@epfl.ch](mailto:philipp.battig@epfl.ch) (P. Bättig), [patrick.wagner@epfl.ch](mailto:patrick.wagner@epfl.ch) (P.H. Wagner), [jurg.schiffmann@epfl.ch](mailto:jurg.schiffmann@epfl.ch) (J. Schiffmann).

## Nomenclature

$b_1$	Ridge width, [m]
$b_2$	Groove width, [m]
$D$	Bearing diameter, [m]
$E$	Rotor material elastic modulus, [Pa]
$F_x$	Bearing force in x direction, [N]
$F_y$	Bearing force in y direction, [N]
$F_{x\_im}$	Imbalance force along x direction, [N]
$F_{y\_im}$	Imbalance force along y direction, [N]
$g$	Gravitational acceleration, [m/s <sup>2</sup> ]
$h$	Gas film thickness, [m]
$h_g$	Gas film thickness in groove region, [m]
$h_{go}$	Groove depth, [m]
$h_r$	Gas film thickness in non-groove region, [m]
$h_{r0}$	Bearing initial clearance, [m]
$I_p$	Polar rotor inertia, [kg·m <sup>2</sup> ]
$I_T$	Transversal rotor inertia, [kg·m <sup>2</sup> ]
$l$	Bearing span, [m]
$l_1$	Distance between bearing 1 mid-plane and mass center, [m]
$l_2$	Distance between bearing 2 mid-plane and mass center, [m]
$L$	Bearing length, [m]
$L_{land}$	Land region length, [m]
$m_r$	Rotor mass, [kg]
$p_a$	Ambient pressure, [Pa]
$P$	Bearing pressure, [Pa]
$r_g$	Rotor radial growth caused by centrifugal force, [m]
$R$	Bearing radius, [m]
$R_i$	Rotor inner diameter, [m]
$R_o$	Rotor outer diameter, [m]
$t$	Time, [s]
$X$	Displacement along x, [m]
$Y$	Displacement along y, [m]
$z$	Axial coordinate

### Greek letters

$\alpha$	Groove width ratio
$\beta$	Groove angle, [°]
$\theta$	Circumferential coordinate, [rad]
$\Lambda$	Bearing number
$\mu$	Gas viscosity, [Pa·s]
$\nu$	Rotor material Poisson's ratio
$\xi$	Rotating angle along x axis, [°]
$\rho$	Rotor material density, [kg/m <sup>3</sup> ]
$\sigma$	Squeeze number
$\psi$	Rotating angle along y axis, [°]
$\Psi$	State variable
$\omega$	Relative angular speed of the smooth and groove parts, [rad/s]
$\omega_h$	Absolute angular speed for the smooth part, [rad/s]
$\omega_o$	Absolute angular speed for the groove part, [rad/s]

### Superscripts

-	Normalized
---	------------

### Subscripts

$a$	Ambient condition
$g$	Groove region
$i$	Inner diameter
$o$	Outer diameter
$r$	Ridge region

<i>x</i>	x-axis
<i>y</i>	y-axis

#### Abbreviations

CAD	Computer aided design
FDM	Finite difference method
FEM	Finite element method
FVM	Finite volume method
HGJB	Herringbone grooved journal bearing
NGT	Narrow groove theory

turbomachinery, since it allows to run them with small tip clearance as suggested by Diehl et al. [10]. The HGJB has been extensively studied both in theory and experiment [11–14]. Malanoski [15] pointed out the excellent stability characteristics of HGJB in comparison to traditional plain gas bearings. In comparison with tilting pad gas bearings, HGJBs feature a much simpler bearing structure, which significantly reduces the difficulty of manufacturing and assembly. So far, HGJBs have been successfully used in gyroscopes [1], turbocompressors [2], and micro gas turbines [5].

Whipple [16] proposed the narrow groove theory (NGT) to predict the static performance of liquid or gas lubricated spiral grooved thrust bearings. The grooves and ridges were assumed to be sufficiently narrow, which leads to a close-to-smooth pressure change across a groove-ridge pair. This approximation significantly reduces the numerical difficulty and computational cost for the modeling of grooved bearings. Muijderman [17,18] modified Whipple's NGT method through considering grooves along a spiral, which applied a conformal mapping method to map a spiral groove pattern into a parallel one. Vohr and Pan [19] proposed an NGT based model for the spiral-grooved, self-acting bearing of arbitrary geometry (parameterized groove shapes), while Vohr and Chow [11] applied this analysis to HGJBs. The governing differential equation was derived under the assumption of isothermal and compressible flow. Since it was difficult to solve the nonlinear differential equation at that time, the differential equation was linearized by applying an infinitesimal perturbation around a static eccentricity to predict the linearized bearing impedance. In addition to the linearization, they applied a separation of variable approach, which limits the model to small eccentricities (1D-NGT). However, there are many cases that violate this assumption e.g., heavy rotors, large imbalances and self-excited motions. Adopting numerical methods such as the finite difference method (FDM) allows to discretize the NGT equation in the circumferential and axial direction and therefore enables to extend the prediction of the HGJB performance to large eccentricities (2D-NGT) [20–22].

In order to assess the validity of the NGT and to capture the effect of a limited number of grooves, methods of direct discretization of the Reynolds equation were investigated. Van der Stegen [23] introduced the FDM to discretize the Reynolds equation directly in order to predict the load capacity of gas-lubricated HGJBs. However, the film discontinuity of the local film thickness due to the grooves cause numerical challenges associated with numerical oscillations [24]. Reddi and Chu [25] introduced the finite element method (FEM) for solving the steady compressible lubrication problem and Bonneau and Absi [26] used the FEM to analyze HGJBs with small number of grooves. Arghir et al. [27] introduced the finite volume method (FVM) to tackle the fluid film thickness discontinuity. Compared to the FDM, both the FEM and the FVM were suggested to avoid the numerical oscillations and to be more efficient [28]. However, for the direct discretization method, the mesh needs to be consistent with the groove distribution [24,29]. Moreover, this method was suggested to be inefficient and inaccurate for the rotating groove case [26,30]. Considering modern groove manufacturing methods, e.g., laser grooving, which allows to manufacture narrow grooves, the NGT has still been widely used in recent works [21,22,31,32].

Jang and Yoon [33] built a nonlinear theoretical model on fluid lubricated herringbone grooved bearings to investigate the difference between the rotating and the stationary groove design. The FEM was adopted to solve the Reynolds equation and the Runge-Kutta method was used to solve the rotor motion equations. However, only the predicted load capacity, i.e., the static performance was validated with experimental data by Hirs [34]. Wang [35,36] investigated the nonlinear and bifurcation characteristics of the HGJBs (stationary grooves) coupled with a flexible rotor. FDM with the successive over relation method was employed to solve the Reynolds equation. Miyanaga and Tomioka [21] built a nonlinear theoretical model of a HGJB rotor system mounted on viscoelastic supports. The study revealed that the viscoelastic support can improve the threshold speed of whirl instability. However, the nonlinear predictions above adopted the traditional time domain integration method, which discretizes the time dependent terms  $\partial p/\partial t$  and  $\partial h/\partial t$  by a backward difference approximation. Larsen and Santos [37] pointed out that the time dependent terms are lagging behind in time for this method because they are based on the previous time step in the integration of the rotor motion equations. Therefore, this method does not reflect the true simultaneously coupled nature of the state variables of the bearing-rotor system [38].

#### 1.1. Nature of issue

Most of the studies mentioned above focus on a linear analysis, which is based on the small perturbation approach. A linear gas bearing model, indifferent from its complexity, can only predict the linear concept threshold speed of instability and cannot forecast the evolution of the orbits when sub-synchronous vibration start to appear [39–41]. Considering gas foil

bearing supported rigid rotor systems, both predictions by Bonello et al. [38] and Larsen et al. [42] suggest the presence of a speed range, where the orbits continuously evolve towards limit cycles after the stable state (orbit converge to equilibrium position). Moreover, Larsen et al. [37] demonstrated that the sub-synchronous vibrations do not only depend on the operating speed, but also depend on the imbalance level. Only a nonlinear theoretical model that couples the fluid film behavior and the equations of motion of the rotor can capture these characteristics. However, the previous nonlinear predictions on rigid rotors supported on HGJBs [21,33,35,36] neither offer an experimental validation of the predicted onset speed of sub-synchronous vibration, nor provide an insight of the orbit evolution until bearing failure when sub-synchronous vibration occurs. This study is the first to introduce the state space methodology to build the nonlinear prediction model of HGJB and the numerical model was successfully validated in detail through experiment. This study is the first to shed light into the orbit evolution from stable to sub-synchronous vibration and ultimately to bearing failure for the HGJB, and offers therefore unprecedented insights into the operation of HGJB supported rotors.

### 1.2. Goals and objective

The goal is a nonlinear prediction tool, which captures the features of the HGJB supported rotor system. The objectives are to (1) build a parametric nonlinear prediction model of the HGJB-rotor system, (2) validate the proposed theoretical model by comparing it with experimental results, (3) investigate the evolution of the self-excited motion with operating speed for the HGJB-rotor system, and (4) study the effect of static load and imbalance load on the response of HGJBs supported rotor.

### 1.3. Scope of the paper

A nonlinear theoretical model of a rigid rotor supported on two HGJBs was implemented using the 2D-NGT. The rigid rotor motion equations were coupled with the bearing model and then transformed into a set of state equations by introducing a state variable  $\bar{\Psi} = \bar{P}\bar{h}$ . The terms on the right-hand side of the state equations, which are independent in time, were discretized by using the FDM in the spatial domain. An implicit integrator with adaptive time step was used to solve the state equations simultaneously. For the experimental validation of the proposed model, a rotor supported on two low stability HGJBs was built and tested. The predicted onset speed of sub-synchronous vibration based on the nonlinear theoretical model are compared with the experimental results. The evolution of the self-excited motions with operating speed were predicted and analyzed. Based on the experimentally validated nonlinear model, both the effects of static load and imbalance load on the rotor responses were investigated.

## 2. Theory

### 2.1. Bearing theoretical model

The NGT, which assumes an infinite number of grooves, was applied to calculate the fluid film pressure distribution within a HGJB. The non-dimensional modified Reynolds equation for the ideal gas can be expressed as follows:

$$\begin{aligned} & \partial_\theta [\bar{P}(f_\theta \partial_\theta \bar{P} + f_c \partial_z \bar{P})] + \partial_z [\bar{P}(f_c \partial_\theta \bar{P} + f_z \partial_z \bar{P})] \\ & + c_s [\sin\beta \partial_\theta (\bar{P}f_s) - \cos\beta \partial_z (\bar{P}f_s)] = \Lambda \partial_\theta (\bar{P}f_v) + \sigma \partial_t (\bar{P}f_v) \end{aligned} \quad (1)$$

The details of the variables in the modified Reynolds equation are shown in Appendix A. Insights into the derivation of this equation can be found in the review article by Gu et al. [43].

**Fig. 1** shows the coordinate system for the HGJB model. Since the NGT was adopted, the pressure does not fluctuate as the rotor rotates. Thus, a coordinate system fixed to the bushing was used. The FDM method was adopted to discretize the modified Reynolds equation in the spatial domain. **Fig. 2** shows the grid and the boundary conditions of the implemented model. The model assumes a perfectly-aligned shaft and ambient pressure at both bearing axial ends. Therefore, the bearing gas pressure distribution is assumed to be symmetrical about the bearing mid-plane. Thus, only half of the bearing is modeled, which significantly reduces the computational cost. Four boundary conditions are applied to constrain the differential equation, which are shown in **Fig. 2** and summarized as follows:

1. The pressure at the bearing axial end ( $j = 1$ ) is equal to the ambient pressure:

$$\bar{P}(\theta, \bar{z} = 0) = 1 \quad (2)$$

2. Periodic boundary conditions are adopted along the circumferential direction:

$$\bar{P}(\theta, \bar{z}) = \bar{P}(\theta + 2\pi, \bar{z}) \quad (3)$$

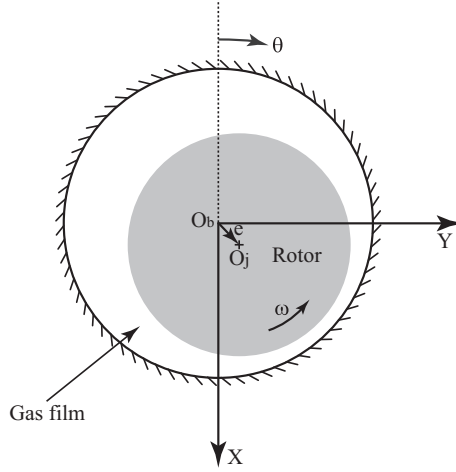


**Fig. 1.** Coordinate system used for the herringbone grooved journal gas bearing model.

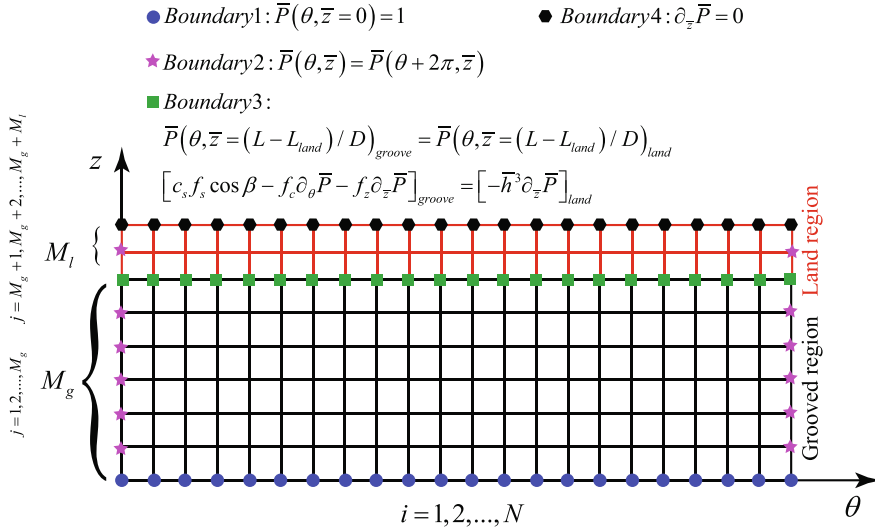


**Fig. 2.** Mesh and boundary condition of the studied HGJB.

3. The pressure at the border between the grooved and the land region is the same and the mass flow continuity needs to be satisfied:

$$\begin{aligned} \bar{P}(\theta, \bar{z} = (L - L_{land}) / D)_{groove} &= \bar{P}(\theta, \bar{z} = (L - L_{land}) / D)_{land} \\ [c_s f_s \cos \beta - f_c \partial_{\theta} \bar{P} - f_z \partial_{\bar{z}} \bar{P}]_{groove} &= [-h^3 \partial_{\bar{z}} \bar{P}]_{land} \end{aligned} \quad (4)$$

4. The mass flow normal to the mid-plane is 0:

$$\partial_{\bar{z}} \bar{P} = 0 \quad (5)$$

HGJBs are typically operated at high rotor speeds and the radial bearing clearance is only a few micrometers to ensure stable operation. The performance of HGJBs is very sensitive to the bearing clearance, therefore the rotor expansion caused by the centrifugal force needs to be taken into consideration. The radial growth of the rotor caused by the centrifugal force can be predicted via the plain stress model of a thin circular disk [44], which can be expressed as follows:

$$r_g = \frac{1}{E} \left[ (1 - \nu) R_0 C_0 - (1 + \nu) \frac{1}{R_0} C_1 - \frac{(1 - \nu^2)}{8} \rho \omega^2 R_0^3 \right] \quad (6)$$

with  $C_0 = ((3 + v)/8)\rho\omega^2(R_i^2 + R_o^2)$ , and  $C_1 = -((3 + v)/8)\rho\omega^2R_i^2R_o^2$ . The variable  $\rho$  represents the rotor material density,  $E$  and  $v$  are the elastic modulus and Poisson's ratio of the rotor material, respectively,  $R_i$  and  $R_o$  are the rotor inner and outer radius, respectively.

The Reynolds equation was solved by using the Newton-Raphson method with successive over-iterations. The calculated gas film pressure distribution allows to determine the non-dimensional bearing forces in the x and y direction:

$$\begin{bmatrix} \bar{F}_X \\ \bar{F}_Y \end{bmatrix} = 2 \int_0^{L/D} \int_0^{2\pi} (\bar{P} - 1) \begin{bmatrix} \cos\theta \\ -\sin\theta \end{bmatrix} d\theta dz \quad (7)$$

## 2.2. Rotor motion equations

**Fig. 3** represents the coordinate system for the investigated rotor system, which is supported on two HGJBs. Since the stiffness of the rotor is much higher than the gas bearing stiffness, the rotor is modeled as a rigid body. The non-dimensional equations of motion of the rotor are as follows:

$$\begin{aligned} \bar{m}_r \ddot{\bar{X}} &= \bar{F}_X^1 + \bar{F}_X^2 + \bar{F}_{X\_im} + \bar{m}_r \bar{g} \\ \bar{m}_r \ddot{\bar{Y}} &= \bar{F}_Y^1 + \bar{F}_Y^2 + \bar{F}_{Y\_im} \\ \bar{I}_T \ddot{\bar{\xi}} + \bar{I}_p \dot{\bar{\psi}} &= \bar{F}_Y \bar{l}_1 - \bar{F}_X \bar{l}_2 + \bar{M}_{\xi\_im} \\ \bar{I}_T \ddot{\bar{\psi}} - \bar{I}_p \dot{\bar{\xi}} &= -\bar{F}_X \bar{l}_1 + \bar{F}_Y \bar{l}_2 + \bar{M}_{\psi\_im} \end{aligned} \quad (8)$$

where  $\bar{m}_r$  is the non-dimensional rotor mass,  $\bar{I}_T$  and  $\bar{I}_p$  are the non-dimensional transversal rotor inertia and the non-dimensional polar rotor inertia,  $\bar{X}$  and  $\bar{Y}$  represent the dimensionless displacement along x and y direction,  $\bar{\xi}$  and  $\bar{\psi}$  represent the dimensionless rotating angle along  $\xi$  and  $\psi$  direction,  $\bar{F}_X$  and  $\bar{F}_Y$  represent the non-dimensional bearing forces in the x and y direction,  $\bar{F}_{X\_im}$  and  $\bar{F}_{Y\_im}$  represent the non-dimensional imbalance forces along the x and y direction,  $\bar{l}$  represents the non-dimensional distance between the bearing mid-plane and the mass center, the superscript or subscript (1 or 2) represents the bearing name.  $\bar{M}_{\xi\_im}$  and  $\bar{M}_{\psi\_im}$  represent the non-dimensional moment caused by the imbalances along the  $\xi$  and  $\psi$  direction, respectively. All the dimensionless variables in Eq. (8) are summarized in Appendix B.

## 2.3. State equations for the coupled bearing rotor system

The traditional nonlinear modeling approach is based on a discretization of the time terms ( $\partial_t \bar{P}, \partial_t \bar{h}$ ) directly by using the backward difference approximation [45]. As mentioned by Larsen and Santos [37], a time lagging is introduced by this method, which requires a small time step to obtain sufficiently-accurate solutions. Bonello and Pham [38,46] introduced an alternative state variable  $\Psi = \bar{P}\bar{h}$ , which avoids the discretization of the time terms. The advantage is that the coupled Reynolds equation and rotor motion equations can be transformed into a set of state equations, which allows to solve the state variables simultaneously. Larsen and Santos [37,42] also adopted this method and validated the rotor response of a foil bearing supported rotor system with experimental data. By introducing the state variable  $\Psi = \bar{P}f_v$ , the modified Reynolds equation Eq. (1) is transformed into the format of a state equation:

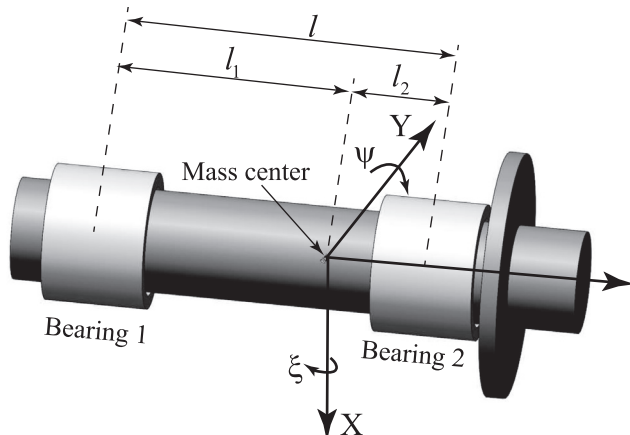


**Fig. 3.** Coordinate system for the studied bearing rotor system.

$$\dot{\Psi} = \frac{1}{\sigma} \left\{ \partial_\theta \left[ \left( \frac{\Psi}{f_v} \right) \left( f_\theta \partial_\theta \left( \frac{\Psi}{f_v} \right) + f_c \partial_z \left( \frac{\Psi}{f_v} \right) \right) \right] + \partial_z \left[ \left( \frac{\Psi}{f_v} \right) \left( f_c \partial_\theta \left( \frac{\Psi}{f_v} \right) + f_z \partial_z \left( \frac{\Psi}{f_v} \right) \right) \right] + c_s \left[ \sin \beta \partial_\theta \left( \left( \frac{\Psi}{f_v} \right) f_s \right) - \cos \beta \partial_z \left( \left( \frac{\Psi}{f_v} \right) f_s \right) - \Lambda \partial_\theta (\Psi) \right] \right\} \quad (9)$$

Using  $\bar{X}_1 = \bar{X}$ ,  $\bar{X}_2 = \dot{\bar{X}}$ ,  $\bar{Y}_1 = \bar{Y}$ ,  $\bar{Y}_2 = \dot{\bar{Y}}$ ,  $\bar{\xi}_1 = \bar{\xi}$ ,  $\bar{\xi}_2 = \dot{\bar{\xi}}$ ,  $\bar{\psi}_1 = \bar{\psi}$ ,  $\bar{\psi}_2 = \dot{\bar{\psi}}$ , the equations of motion of the rotor (Eq. (8)) can be transformed into the format of state equations as follows:

$$\begin{bmatrix} \dot{\bar{X}}_1 \\ \dot{\bar{X}}_2 \\ \dot{\bar{Y}}_1 \\ \dot{\bar{Y}}_2 \\ \dot{\bar{\xi}}_1 \\ \dot{\bar{\xi}}_2 \\ \dot{\bar{\psi}}_1 \\ \dot{\bar{\psi}}_2 \end{bmatrix} = \begin{bmatrix} \bar{X}_2 \\ \left( \bar{F}_X^1 + \bar{F}_X^2 + \bar{F}_{X\_im} + \bar{m}_r \bar{g} \right) / \bar{m}_r \\ \bar{Y}_2 \\ \left( \bar{F}_Y^1 + \bar{F}_Y^2 + \bar{F}_{Y\_im} \right) / \bar{m}_r \\ \bar{\xi}_2 \\ \left( \bar{F}_Y \bar{l}_1 - \bar{F}_Y \bar{l}_2 + \bar{M}_{\xi\_im} - \bar{I}_p \bar{\psi}_2 \right) / \bar{I}_T \\ \bar{\psi}_2 \\ \left( -\bar{F}_X \bar{l}_1 + \bar{F}_X \bar{l}_2 + \bar{M}_{\psi\_im} + I_p \bar{\xi}_2 \right) / \bar{I}_T \end{bmatrix} \quad (10)$$

The state variables, which include the product of gas film pressure and gas film thickness ( $\Psi = \bar{P} f_v$ ), the rotor motion velocities ( $\dot{\bar{X}}, \dot{\bar{Y}}, \dot{\bar{\xi}}, \dot{\bar{\psi}}$ ) and the rotor motion displacements ( $\bar{X}, \bar{Y}, \bar{\xi}, \bar{\psi}$ ), are solved simultaneously by coupling Eqs. (9) and (10). An implicit integrator with adaptive time step was adopted to integrate all the state equations [47].

### 3. Model validation

Wagner et al. optimized [48] and tested [49] an oil-free steam-driven recirculation fan for the application in solid oxide fuel cell systems. In preliminary tests, the rotor was operated in hot air at 220 °C, up to 168 krpm. Wagner et al. [50] coupled the recirculation fan to an actual fuel cell system, where the turbine was propelled by steam, the bearings were steam-lubricated and rotational speeds of up to 220 krpm were reached. Fig. 4(a) shows the rotor of that fan: on the left the steam turbine, in the middle the rotor with two HGJBs, and on the right the radial fan with the single-sided spiral-grooved thrust bearing. These three parts were connected by a tie-bolt and then locked by a nut. Note that for the test with fuel cell in the

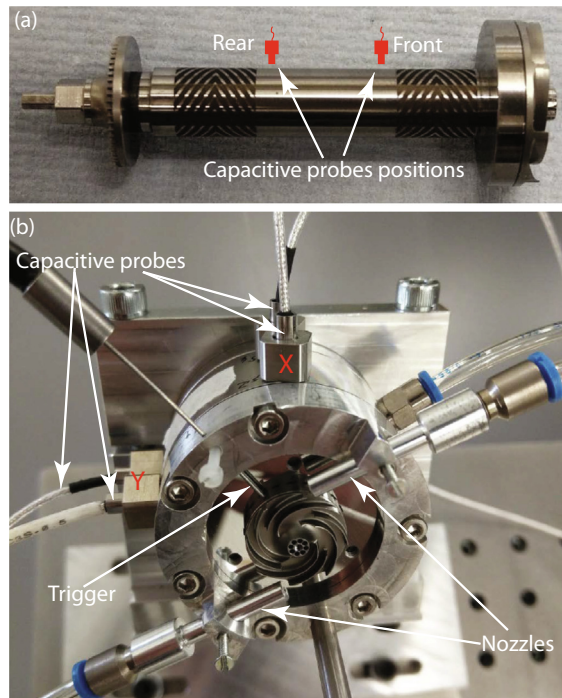


**Fig. 4.** (a) Rotor of the anode off-gas recirculation fan for the application in solid oxide fuel cell system and; (b) installation of the test rig with two capacitive displacement probes (Lion Precision C3S), one trigger (Philtac D20), and two air nozzles to drive the shaft.

relevant environment, the rotor was installed vertically (axial load of 0.27 N). In this study, the experimental setup is shown in Fig. 4(b), where the rotor is mounted at 45°, instead of the nominal value of 90°. A rotor with two low stability HGJBs was used for this investigation, which allows to observe self-excited motions (sub-synchronous vibration) at relatively low speeds. The shaft was propelled by the fan with pressurized air injected by two nozzles, rather than by the turbine. Table 1 lists the details of the bearing and the rotor nominal parameters. The exact parameter definition is given in Appendix A and in Fig. A1. Since the radial bearing clearance has a significant impact on the stability, it was verified with dimensional measurements (measurement uncertainty of  $\pm 0.4 \mu\text{m}$ ). The groove profile was measured through the roughness meter TESA Rugosurf 90G to confirm the manufacturing accuracy. The measurement results suggest insignificant errors on the groove width ratio and a  $\pm 1 \mu\text{m}$  uncertainty on the groove depth. The groove angle was measured with a microscope HiROX KH-8700, suggesting insignificant deviation compared to the design value. More details on those measurements are summarized in Appendix C. Two pairs of perpendicularly installed capacitive displacement sensors (Lion Precision C3S) were used to measure the displacement at the left side of the front bearing and the right side of the rear bearing, respectively (see Fig. 4(a)).

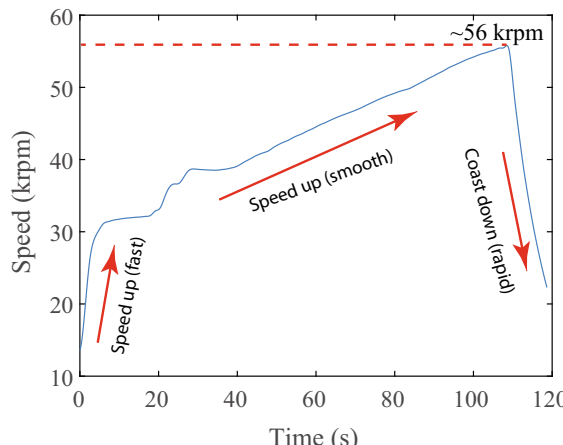
In order to protect the test rig during the experimentations, the rotor speed was increased smoothly and slowly until the sub-synchronous vibrations start to occur. The pressurized air supply was interrupted as soon as the sub-synchronous vibrations occurred, leading to a free rotor coast down. Fig. 5 shows a typical evolution for the whole test process. Below 30 krpm, the speed was increased quickly to ensure a rapid bearing lift-off to avoid too much dry friction between the bushings and the shaft. In the following, the speed was increased up to  $\sim 56$  krpm, the speed at which clear sub-synchronous vibration was detected. The rotor coast down period only lasts for  $\sim 10$  s due to the large windage loss of the turbine and the fan. Since the coast down period is very short, only the data during the speed up period was used for the analysis.

Fig. 6 shows the waterfall plots for all four displacement sensors. It suggests the onset speed of sub-synchronous vibrations is at  $\sim 53$  krpm. Above this speed, the sub-synchronous amplitudes of the four probes increase rapidly up to  $\sim 0.3 \mu\text{m}$  (front probes) as the rotor speed is increased. For all four probes the whirl speed ratio (ratio between sub-synchronous and rotational frequencies) is  $\sim 0.4$ . Before the sub-synchronous vibrations occur, the main vibrations are synchronous, showing constant amplitude of  $\sim 0.4 \mu\text{m}$  and  $\sim 0.2 \mu\text{m}$  for the front bearing and rear bearing, respectively. Clear multi-synchronous

**Table 1**

Nominal parameters of the bearing and rotor for the tested rotor system (bold values were validated with measurements, non-formatted values were extracted from the CAD model).

Bearing diameter	<b>8 mm</b>
Bearing length	<b>8 mm</b>
Groove width ratio	<b>0.65</b>
Groove angle	<b>146.2°</b>
Groove depth	<b>13.6 <math>\mu\text{m}</math> (<math>\pm 1 \mu\text{m}</math>)</b>
Number of grooves	<b>16</b>
Radial bearing clearance	<b>8.4 <math>\mu\text{m}</math> (<math>\pm 0.4 \mu\text{m}</math>)</b>
Rotor mass	<b>0.0271 kg</b>
Polar rotor inertia	<b><math>6.073e-7 \text{ kgm}^2</math></b>
Transversal rotor inertia	<b><math>7.782e-6 \text{ kgm}^2</math></b>
Distance between rear bearing mid-plane and rotor mass center	16.13 mm
Distance between front bearing mid-plane and rotor mass center	8.65 mm



**Fig. 5.** Speed map during the whole speed up and coast down period.

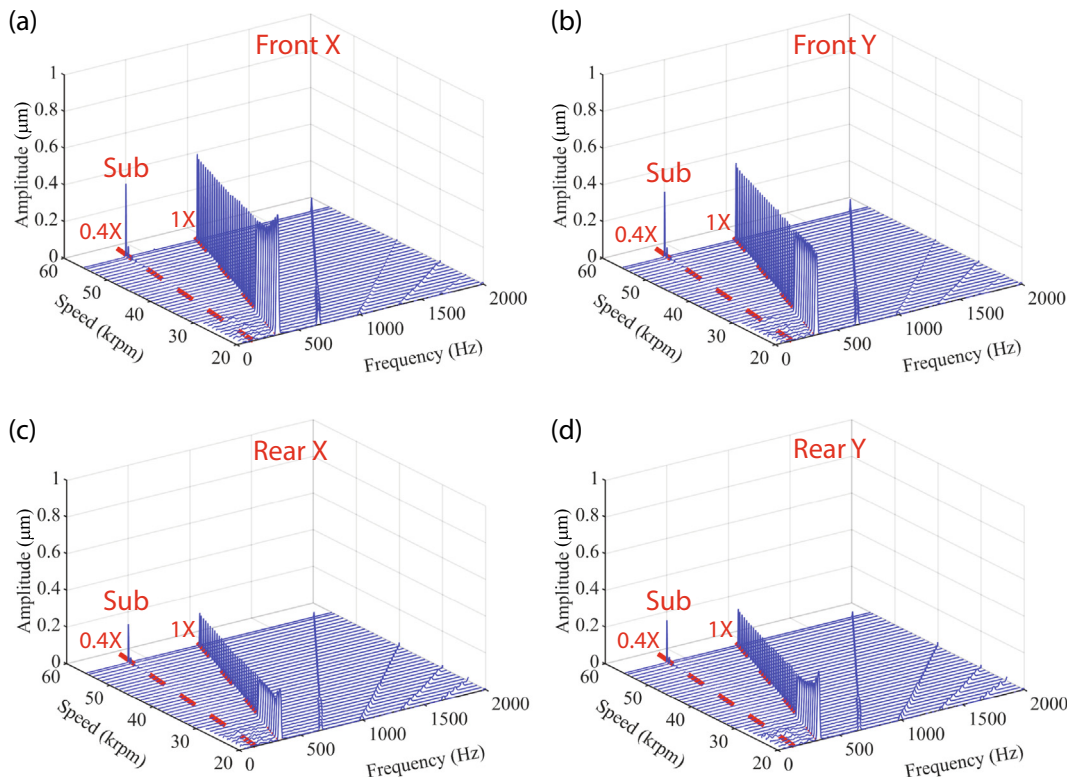


**Fig. 6.** Waterfall plots of the radial displacement measured by four capacitive probes: (a) front X; (b) front Y; (c) rear X; and (d) rear Y.

components were also shown during the whole process. The synchronous amplitude is relatively small compared to the bearing clearance (<10%) because the residual imbalance was reduced to a minimum (estimated to be 5.4 mgmm at the front and 2.7 mgmm at the rear).

Fig. 7(a) shows the predicted dimensionless rotor response at the front bearing mid-plane in x direction ( $e_x$ ) with no imbalance obtained by incrementally increasing the speed by 1 krpm, starting from 10 krpm and by applying the nominal rotor and bearing parameters. Up to 37 krpm, the response decays to one static eccentricity, which corresponds to the equilibrium position. As the speed increases to 38 krpm, the response remains stable, but does not decay to one point anymore, which indicates a limit cycle with a sub-synchronous component [42]. The spectral analysis in Fig. 7(b) suggests a whirl frequency ratio of ~0.4, which agrees well with the experimental result (~0.4, Fig. 6). The temperature rise and the thermal deformation are assumed to be negligible for the test rig under the operating conditions in this study because of (1) the extremely small heat generation from the bearings (on the order of 2 Watt) and (2) the very good heat dissipation around the bearings. Thus, the isothermal assumption was adopted in the simulation. The prediction in Fig. 7, however, does not account for possible deviations of the bearing dimensions with respect to the nominal parameters. According to the bearing geometry dimensional measurements (Table 1), the bearing clearance and groove depth vary within the uncertainty ( $\pm 0.4 \mu\text{m}$  and  $\pm 1 \mu\text{m}$ , respectively). Guenat and Schiffmann [51] suggested that these two parameters yield the most significant influence on the HGJB performance. Fig. 8 shows the predicted onset speed of sub-synchronous vibration for four cases of deviations: (a)  $h_{r0} + 0.4 \mu\text{m}$  and  $h_{go} + 1 \mu\text{m}$ , (b)  $h_{r0} + 0.4 \mu\text{m}$  and  $h_{go} - 1 \mu\text{m}$ , (c)  $h_{r0} - 0.4 \mu\text{m}$  and  $h_{go} + 1 \mu\text{m}$ , and (d)  $h_{r0} - 0.4 \mu\text{m}$  and  $h_{go} - 1 \mu\text{m}$ , where  $h_{r0}$  and  $h_{go}$  are the nominal bearing radial clearance and groove depth, respectively. The onset speed of sub-synchronous vibration varies between 32 krpm and 48 krpm, confirming a high impact of the studied parameters (bearing clearance and groove depth). The upper limit of the error band (48 krpm) correlates within 10% to the experimental results (~53 krpm). Considering the high sensitivity of the bearing dynamic performance to the bearing geometry [14,52], the difference in onset speed of sub-synchronous vibration between the nonlinear model and the experiment data is considered small. It should be noted that the deviation of other parameters, such as the rotor and bushing cylindricity (in the order of 1  $\mu\text{m}$ ), the rotor imbalance, and the rotor misalignment are not considered in the predictions, which certainly increase the uncertainty. Besides the manufacturing deviation, the NGT assumption adopted in this manuscript may be another reason for the deviation between the numerical and experimental data, although recent work by Iseli et al. [53] suggested that the NGT is very accurate for the bearings investigated in this work when compared to more complex modeling approaches, e.g., an FEM method. Thus, it is assumed that a 10% (upper limit) to 30% (nominal) error on the prediction of the

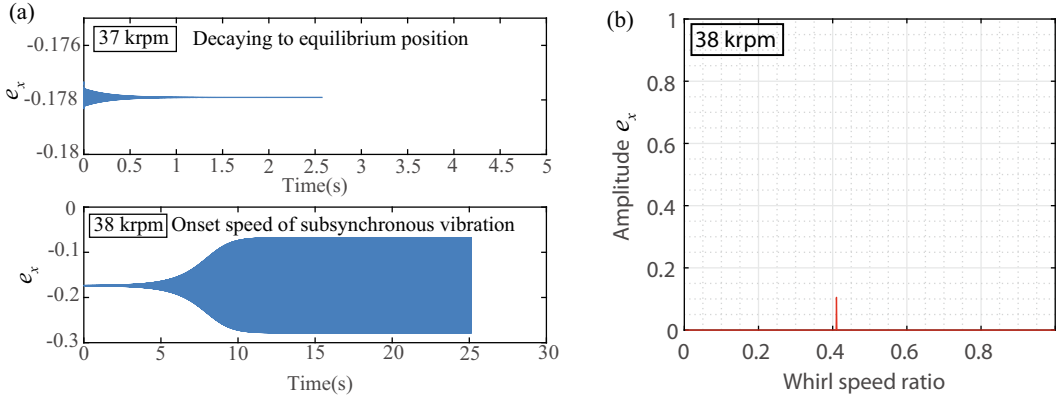


**Fig. 7.** Predicted rotor response at the front bearing mid-plane in x direction near the onset speed of sub-synchronous vibrations.

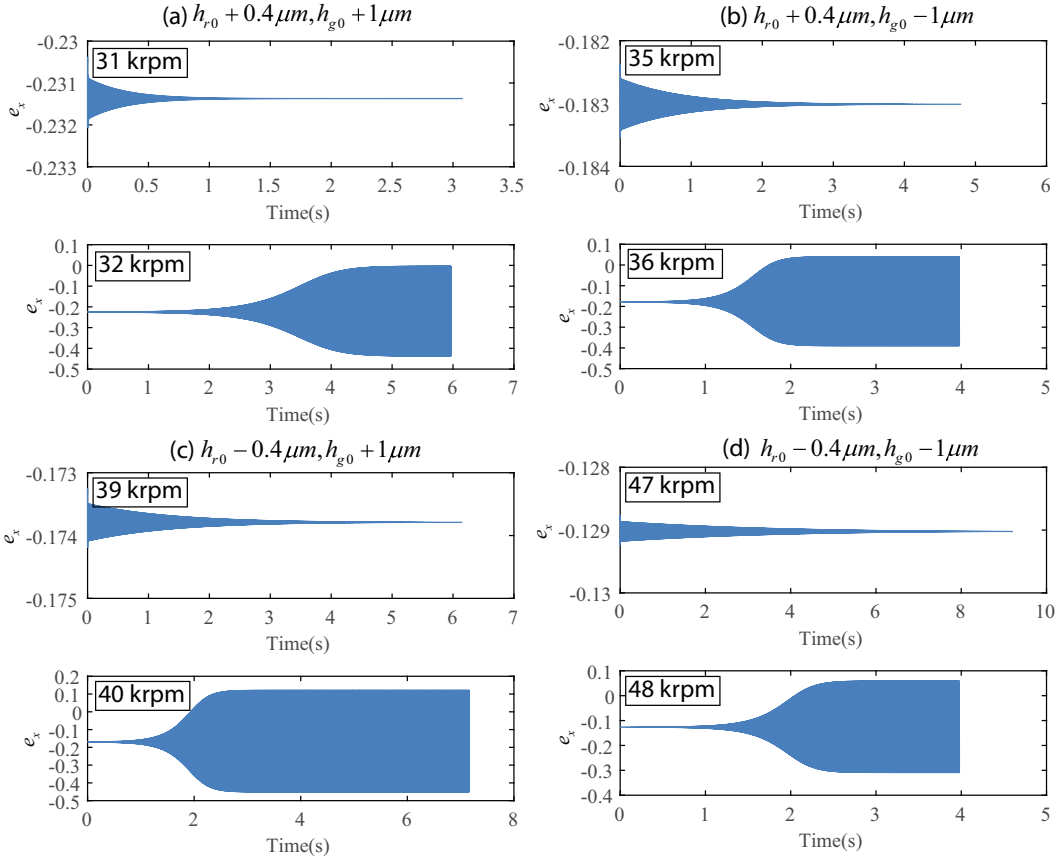


**Fig. 8.** Predicted onset speed of sub-synchronous vibration when considering the bearing clearance and groove depth deviations. (a)  $h_{r0} + 0.4 \mu\text{m}$  and  $h_{g0} + 1 \mu\text{m}$ ; (b)  $h_{r0} + 0.4 \mu\text{m}$  and  $h_{g0} - 1 \mu\text{m}$ ; (c)  $h_{r0} - 0.4 \mu\text{m}$  and  $h_{g0} + 1 \mu\text{m}$ ; and (d)  $h_{r0} - 0.4 \mu\text{m}$  and  $h_{g0} - 1 \mu\text{m}$ .

onset speed of sub-synchronous vibration and the good agreement on whirl speed ratio are sufficient to validate the nonlinear model proposed in this work.

Since neither imbalance nor external loads were considered in the simulation above, the reason for the sub-synchronous vibration is suggested to be self-excitation. Due to risk mitigation, the evolution of the self-excited motion with rotor speed were studied with simulations based on the proposed nonlinear model, rather than with (expensive) experiments. This allows to investigate the process from the start of the self-excited motion to the bearing failure. Fig. 9 shows the evolution of the rotor responses at the front bearing after the onset speed of the sub-synchronous vibration evaluated with nominal

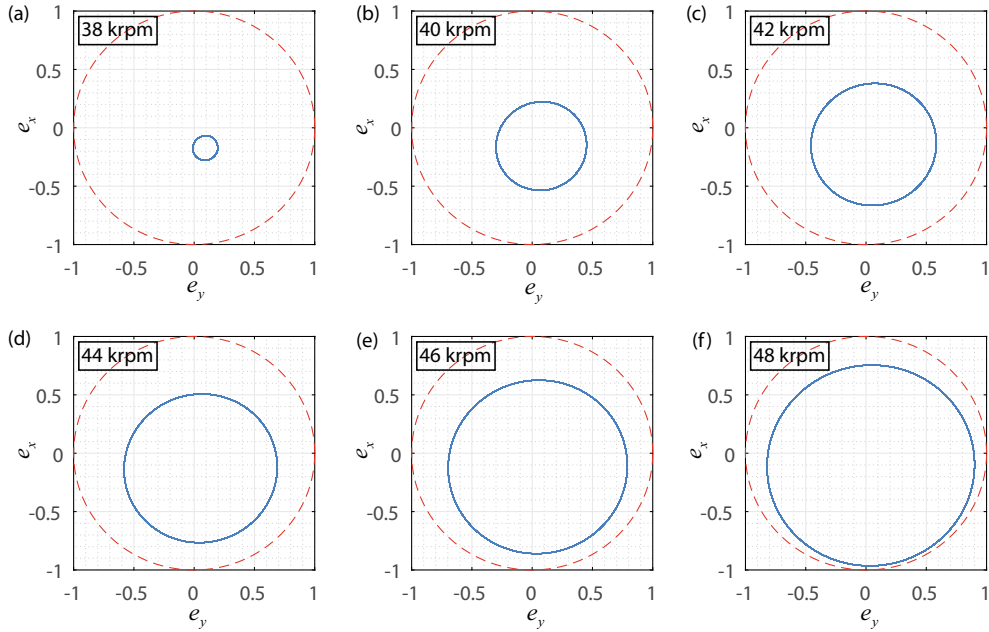


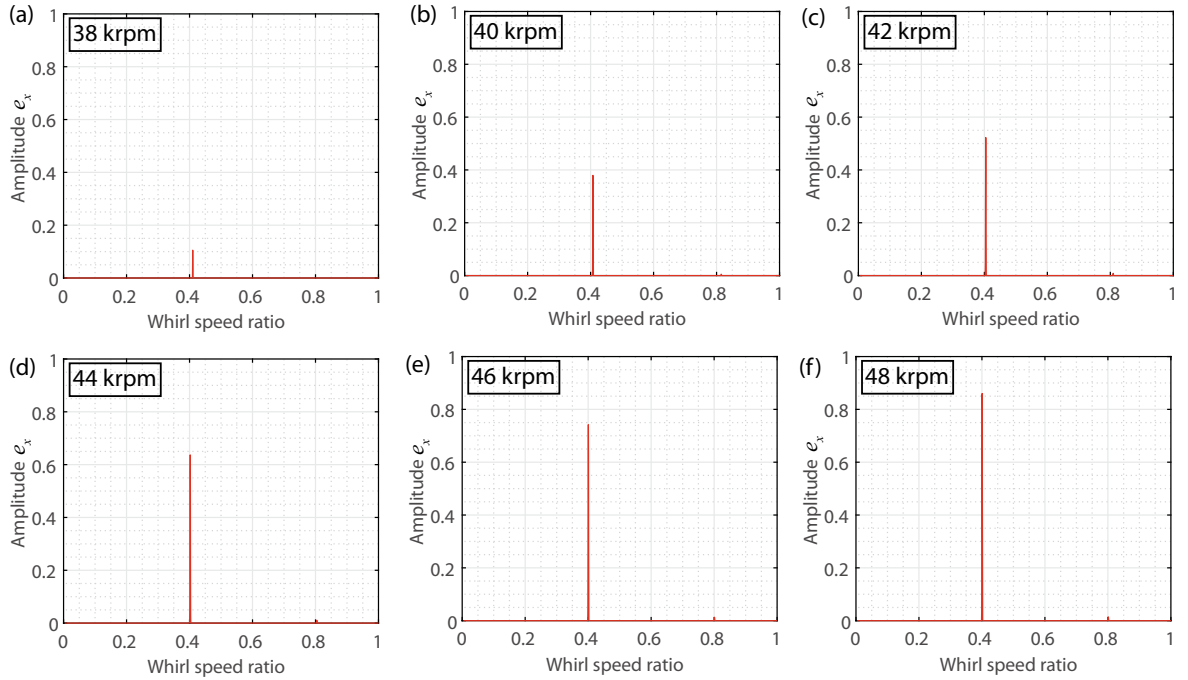
**Fig. 9.** Predicted rotor responses (solid blue line) without imbalance at the front bearing for six different speeds after the onset speed of sub-synchronous vibrations. (a) 38 krpm; (b) 40 krpm; (c) 42 krpm; (d) 44 krpm; (e) 46 krpm; and (f) 48 krpm. The red dashed line represents the bearing surface. (For interpretation of the references to colour in this figure legend, the reader is referred to the web version of this article.)

rotor and bearing parameters. The blue solid line represents the predicted rotor orbit and the red dashed line represents the bushing surface. As suggested in Fig. 7, the orbits decay to an equilibrium position, if the speed is lower than 38 krpm. If the speed increases to 38 krpm, a limit cycle with a small amplitude appears (Fig. 9(a)), which indicates the start of the self-excited motion. The limit cycle increases rapidly at the beginning and then progresses slowly, when the rotor approaches the bearing surface. At a speed of 48 krpm, the rotor orbit is close to the bearing surface, which indicates a high risk of bearing failure. At 49 krpm, the simulation fails because of contact between the rotor and the bushing. It is interesting to note that in this case, the reason for the failure is not due to an unstable rotor behavior, since the rotor orbit is still bound by a limit cycle at 48 krpm. The failure rather occurs because the amplitude of the limit cycle grows beyond the nominal bearing clearance due to a dropping of the overall effective damping of the present vibration mode. These observations suggest that it might be useful to distinguish among three distinct threshold speeds:

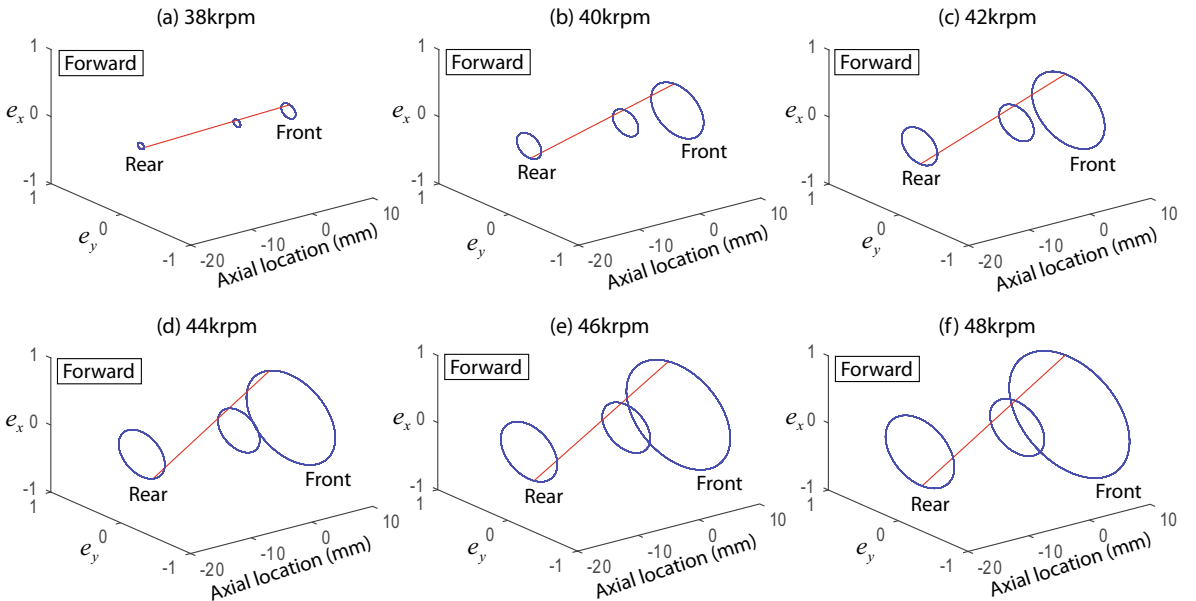
1. Onset speed of sub-synchronous vibration: Rotor speed at which first signs of the sub-synchronous vibration start to occur due to a decreasing overall effective damping.
2. Bearing failure speed: Rotor speed at which rotor touchdown occurs due to either a too large limit cycle amplitude or due to a bearing instability.
3. Threshold speed of instability: Rotor speed at which the rotor orbit increases exponentially due to a negative overall effective damping.

Fig. 10 shows the spectral analysis of the limit cycles in Fig. 9. Only the results in x direction are shown, since the results in y direction are similar. The x-axis corresponds to the whirl speed ratio, which is the ratio of the self-excited frequency and the rotor rotating frequency. The y-axis represents the dimensionless 0-peak amplitude of the rotor responses in x direction ( $e_x$ ). The amplitude increases rapidly after the first occurrence of sub-synchronous motion and then more slowly at higher speeds, which is consistent with the analysis on the limit cycles in Fig. 9. The dimensionless 0-peak amplitude is only 0.11 at 38 krpm, while it increases to 0.86 at 48 krpm. The whirl speed ratio remains almost constant at ~0.4 as the rotor speed increases from 38 krpm to 48 krpm (whole self-excited motion period). This agrees very well with the experimental results, which show a whirl speed ratio of 0.4 (Fig. 6).

Fig. 11 shows the predicted mode shape of the self-excited motions for the six rotor speeds analyzed above. The three orbits represent the orbit of the rear bearing (left bearing), the mass center (middle), and the front bearing (right). At the onset speed of sub-synchronous vibration, the three orbits are all relatively small. With increasing speed, the three orbits increase simultaneously. The rear bearing orbit is smaller than the front one at all investigated speeds, which indicates a bearing failure may happen first at the front due to the increased self-excited motion. This phenomenon is consistent with the experimental results, which show larger sub-synchronous amplitudes at the front bearing (Fig. 6). Fig. 11 clearly suggests that the conical mode dominates the sub-synchronous rotor motion for all the speeds rather than the cylindrical one. This



**Fig. 10.** Spectral analysis at the front bearing in x direction for six different speeds after the onset speed of sub-synchronous vibrations. (a) 38 krpm; (b) 40 krpm; (c) 42 krpm; (d) 44 krpm; (e) 46 krpm; and (f) 48 krpm.



**Fig. 11.** Mode shape predicted for six different speeds after the onset speed of sub-synchronous vibrations using the non-linear model. (a) 38 krpm; (b) 40 krpm; (c) 42 krpm; (d) 44 krpm; (e) 46 krpm; and (f) 48 krpm.

indicates that the self-excited motion originate from the conical mode natural frequency in this case. Moreover, the self-excited conical motions are all forward conical motions.

In summary, the onset speed of sub-synchronous vibration, the whirl frequency ratio, and the mode shapes of the self-excited motions predicted by the nonlinear model corroborate with the experimental results, which therefore validates the implemented nonlinear rotor-bearing model.

#### 4. Effect of static load on rotor response

The rotor responses studied above correspond to the case where the rotor is inclined by  $45^\circ$ . In order to investigate the effect of static load on the system stability, the cases of a vertically ( $90^\circ$ ) and horizontally ( $0^\circ$ ) installed rotor were investigated. Fig. 12 shows the predicted onset speed of sub-synchronous vibrations for the vertically installed rotor (Fig. 12(a)) and the horizontally installed rotor (Fig. 12(b)), respectively. The vertical rotor response decays to an equilibrium position at 35 krpm, and starts to present self-excitation motions at 36 krpm. This indicates a reduced level of stability compared to the  $45^\circ$  inclined rotor. However, it should be noted that the HGJB-rotor system can operate in a stable manner even if the rotor is vertically installed. This was experimentally demonstrated in Refs. [49,50] for a similar setup. A vertically-mounted rotor was operated up to the design operating speed of 168 krpm without any sub-synchronous vibration. This is impossible for a circular plain bearing rotor system, because of its inherent instability when the bearing is unloaded [54]. The onset speed of sub-synchronous vibrations of the horizontal rotor increases to 40 krpm, which is higher than both the vertically and  $45^\circ$  inclined rotor, suggesting, therefore, that static load delays the appearance of sub-synchronous vibrations.

Fig. 13 shows the predicted onset speed of sub-synchronous vibrations for different static loads applied to the rotor mass center. The static load is increased from 0 to four-times the rotor weight ( $4m_r g$ ). The results suggest an increase in the onset speed of sub-synchronous vibrations from 36 krpm to 75 krpm as the static load increases from 0 to  $4m_r g$ . As the static load increases, the static rotor eccentricity becomes larger, which increases the dynamic stiffness of the bearing and decreases the cross-coupling behavior, which corroborates with analyses presented by Iseli et al. [53]. Thus, the natural frequency of the

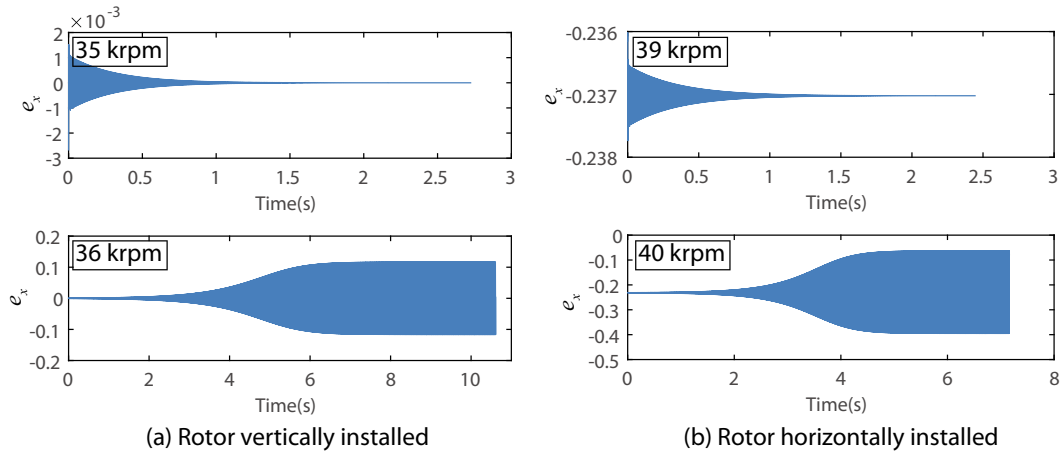


**Fig. 12.** Onset speed of sub-synchronous vibrations for rotor (a) vertically and (b) horizontally inclined.

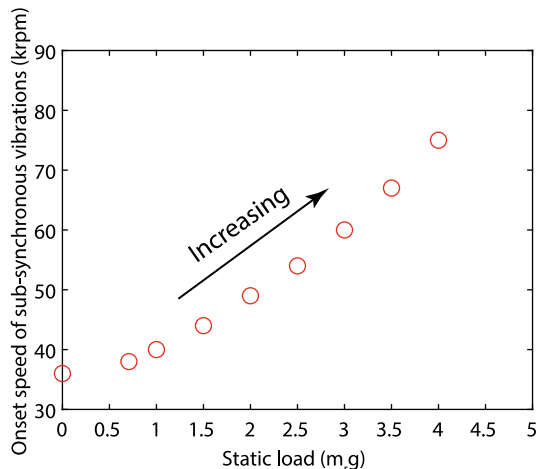


**Fig. 13.** Effect of static load on the onset speed of sub-synchronous vibrations.

bearing-rotor system increases, which leads to higher onset speed of sub-synchronous vibration. The onset speed of sub-synchronous vibration increases slowly at low static loads, while it increases more rapidly at higher static loads. These results suggest that the HGJB stability can be improved by increasing the static load applied on the bearings. However, the lift-off speed will also increase with the static load, which will aggravate the dry friction and potential wear during start-stop periods. Moreover, the power loss will also increase due to the thinner film thickness.

## 5. Effect of imbalance on the response

The analysis above are based on a perfectly balanced rotor, while residual imbalances always exist in real applications. In order to assess the effect of imbalance, imbalances of 20 mgmm, 30 mgmm, and 40 mgmm were added at the rotor mass center position. Fig. 14 shows the evolution of the rotor response with an imbalance of 20 mgmm for different speeds after

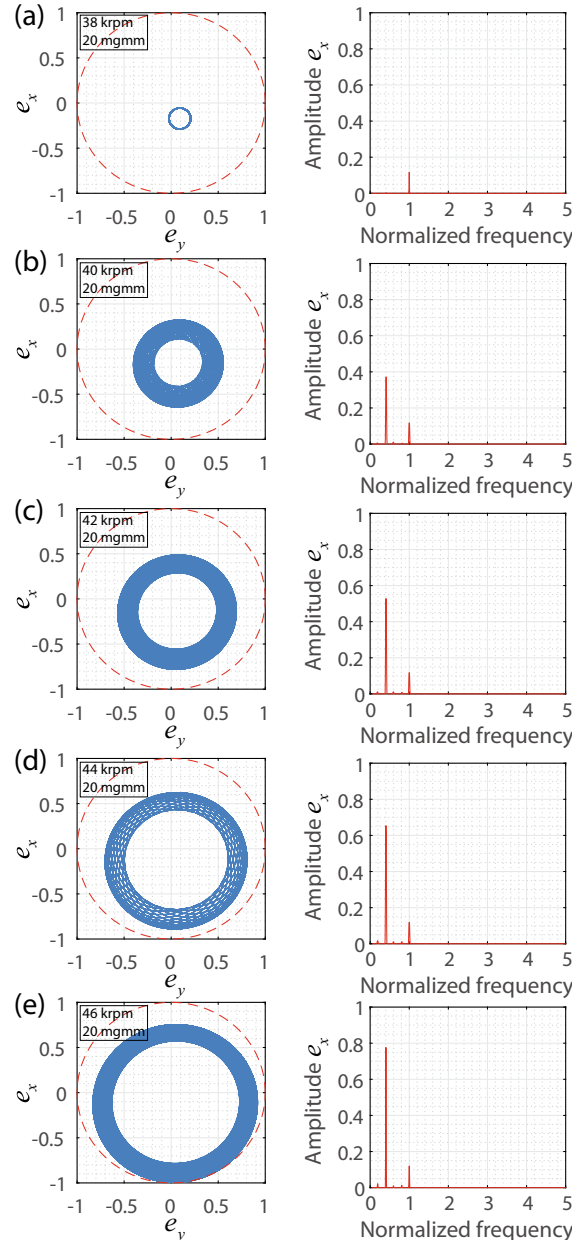


**Fig. 14.** Rotor responses with 20 mgmm imbalance located at the rotor mass center from 38 krpm to 46 krpm.

the occurrence of the self-excited motion, which was from 38 krpm to 46 krpm (rotor inclined by 45°). Unlike the rotor responses in Fig. 9, which only shows circular limit cycles, the rotor responses with added imbalance shows complex orbits except at 38 krpm, where the rotor orbit is circular, which is similar to the orbit of the rotor with no imbalance excitation in Fig. 9(a). However, the frequency spectrum in Fig. 14(a) only shows amplitudes at the synchronous frequency whereas the no-imbalance excitation case only shows sub-synchronous frequency (Fig. 10(a)), therefore suggesting that imbalance can delay the onset of the sub-synchronous vibration. Increasing the imbalance leads to higher transient eccentricity ratio of the shaft center. Thus, the transient natural frequency of the bearing-rotor system increases, which in turn increases the onset speed of sub-synchronous vibration in a similar manner as an increased static load. As the rotor speed increases to 40 krpm, the orbit starts to show more complex shapes. Two frequency components appear in the frequency spectrums of all investigated operating speeds. One of the frequencies is equal to the operating speed, i.e., the synchronous frequency, which is excited by the imbalance forces. Another frequency at ~0.4 times of the operating speed corresponds to self-excited motion. Similar to the results in Fig. 10, the amplitudes of this frequency component increase rapidly as the speed increases, while the synchronous component amplitudes remain almost constant. The orbit is close to the bearing surface at a speed of 46 krpm. At 47 krpm, the simulation fails because of contact between the rotor and the bearing. The speed of bearing failure decreases from 49 krpm to 47 krpm when the 20 mgmm imbalance is considered, since the total rotor response corresponds to the superposition of the self-excited motion and the imbalance-excited motion.

Fig. 15 shows the rotor responses when the imbalance increases to 30 mgmm. The dimensionless synchronous amplitude increases from ~0.12 to ~0.18 for all the rotor speeds compared to the 20 mgmm case, while the sub-synchronous amplitudes are not influenced much. Similar to the case with 20 mgmm imbalance, only the synchronous frequency component appears in the spectral analysis at 38 krpm. Increasing the speed to 45 krpm, the simulation fails because of contact between the

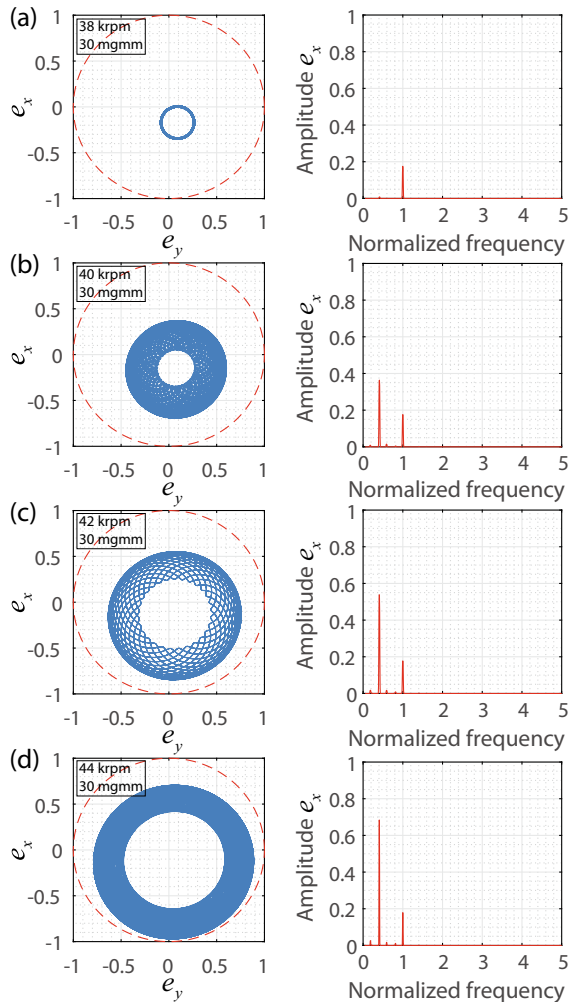


**Fig. 15.** Rotor responses with 30 mgmm imbalance located at the rotor mass center from 38 krpm to 44 krpm.

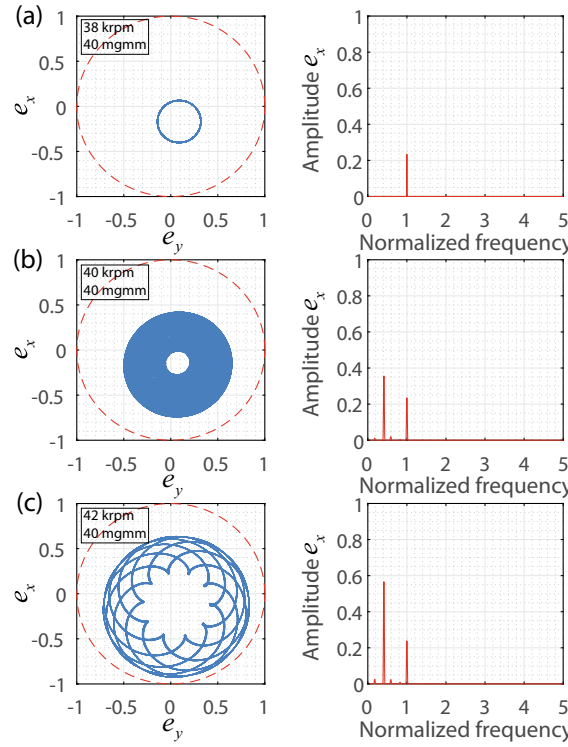


**Fig. 16.** Rotor responses with 40 mgmm imbalance located at the rotor mass center from 38 krpm to 42 krpm.

rotor and the bearing surface. In comparison to the 20 mgmm case, the speed of bearing failure decreases from 47 krpm to 45 krpm, since the synchronous amplitude increases while the sub-synchronous amplitude does not change much. Fig. 16 shows the rotor responses with an imbalance of 40 mgmm. Compared to the 20 mgmm and 30 mgmm cases, the synchronous amplitudes increase to ~0.23, while the speed of bearing failure decreases to 43 krpm. The nonlinear simulation results clearly suggest that the imbalance increases the onset speed of sub-synchronous vibrations, while it reduces the bearing failure speed continuously. Thus, the speed range between the onset speed of sub-synchronous vibrations and the bearing failure speed becomes narrower as the imbalance increases, which make experimental investigations more risky.

## 6. Conclusion

A nonlinear prediction model of a rigid rotor supported on herringbone grooved journal gas bearings (HGJBs) was proposed in this study. The theoretical model couples the bearing model based on the two dimensional narrow groove theory (2D-NGT) with the rotor motion equations. The coupled Reynolds equation and rotor motion equations were transformed into a set of state equations and integrated by an implicit integrator with adaptive time step. A rigid rotor supported on two HGJBs was tested. The speed up and coast down test was conducted to find the onset speed of sub-synchronous vibrations. The proposed theoretical model successfully captured the onset speed of sub-synchronous vibrations in the experiment within 10% to 30% error considering dimensional deviations due to the manufacturing and measurement uncertainty. The evolution of the self-excited motion was investigated as the rotor speed increased after the onset speed of sub-synchronous vibration. The limit cycle continuously increases with rotor speed until bearing failure. The spectral analysis on the limit cycle suggests a whirl speed ratio of ~0.4, which agrees well with the experimental results. The mode shape analysis shows self-excited forward conical mode shapes for all investigated rotor speeds.

The simulation results suggest stable rotor operation even for a vertically inclined rotor, which demonstrates the inherent stability characteristic of the HGJB compared to plain bearing. The results further suggest that increasing the static load increases the onset speed of sub-synchronous vibrations. However, it should be noted that the increased static load also increases both the lift-off speed (higher bearing wear) and the bearing power loss.

When considering rotor imbalances, the non-linear model suggests the appearance of both synchronous and sub-synchronous frequency components. The whirl frequency ratio is nearly independent on the imbalance level. The imbalance analysis shows that the onset speed of sub-synchronous vibrations increases, while the bearing failure speed decreases with

imbalance. This means the speed range from the onset speed of sub-synchronous vibrations to the bearing failure becomes narrower, hence, the bearing failure occurs more rapidly.

The non-linear model allows to analyze the rising limit cycles due to the reduction of the overall effective damping until bearing failure as a function of static and imbalance loads. The results suggest that it might be beneficial to distinguish among (1) onset speed of sub-synchronous vibration, (2) bearing failure speed and (3) threshold speed of instability, which represent three distinct phenomena. The non-linear model of the rotor investigated in this work show that bearing failure occurs before the rotordynamic instability occurs, due to the rising orbit of the self-excited limit cycle.

### CRediT authorship contribution statement

**Wanhui Liu:** Conceptualization, Methodology, Software, Validation, Investigation, Writing - original draft, Writing - review & editing. **Philipp Bättig:** Validation, Investigation, Writing - review & editing. **Patrick H. Wagner:** Validation, Investigation, Writing - review & editing. **Jürg Schiffmann:** Methodology, Writing - review & editing, Project administration, Resources, Supervision, Funding acquisition.

### Declaration of Competing Interest

The authors declare that they have no known competing financial interests or personal relationships that could have appeared to influence the work reported in this paper.

### Acknowledgement

The authors acknowledge the financial support from Innosuisse (26846.2 PFIW-IW). The authors would also like to acknowledge the fruitful discussions with Prof. Ilmar Santos, Dr. Lili Gu, and Dr. Elliott Guenat.

### Appendix A

Fig. A1 shows the physical meaning of the HGJB parameters. In the modified Reynolds equation for HGJBs, the expression of the variables are as follows:

$$f_\theta = \frac{g_1 + g_2 \cos^2 \beta}{g_3} \quad (\text{A1})$$

$$f_z = \frac{g_1 + g_2 \sin^2 \beta}{g_3} \quad (\text{A2})$$

$$f_c = \frac{g_2}{g_3} \sin \beta \cos \beta \quad (\text{A3})$$

$$f_s = \frac{\bar{h}_g^3 - \bar{h}_r^3}{g_3} \quad (\text{A4})$$

$$f_v = \alpha \bar{h}_g + (1 - \alpha) \bar{h}_r \quad (\text{A5})$$

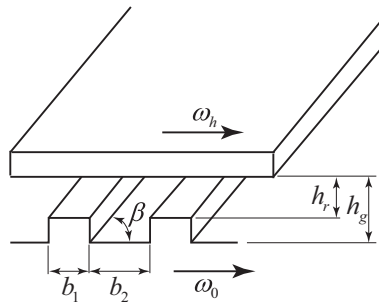


**Fig. A1.** Schematic of the herringbone grooved gas bearing.

$$g_1 = \bar{h}_r^3 \bar{h}_g^3 \quad (\text{A6})$$

$$g_2 = \alpha(1 - \alpha) \left( \bar{h}_g^3 - \bar{h}_r^3 \right)^2 \quad (\text{A7})$$

$$g_3 = (1 - \alpha)\bar{h}_g^3 + \alpha\bar{h}_r^3 \quad (\text{A8})$$

$$c_s = \frac{6\mu(\omega_h - \omega_0)}{p_a} \left( \frac{R}{h_{r0}} \right)^2 \alpha(1 - \alpha) \bar{\delta} \sin \beta \quad (\text{A9})$$

$$\Lambda = \frac{6\mu(\omega_h + \omega_0)}{p_a} \left( \frac{R}{h_{r0}} \right)^2 \quad (\text{A10})$$

$$\sigma = \frac{12\mu\omega}{p_a} \left( \frac{R}{h_{r0}} \right)^2 \quad (\text{A11})$$

$$\bar{\delta} = \frac{h_g - h_r}{h_{r0}} \quad (\text{A12})$$

Here,  $h_{r0}$  is the bearing initial clearance,  $\bar{h}_r = h_r/h_{r0}$  and  $\bar{h}_g = h_g/h_{r0}$  are the non-dimensional gas film thickness in the non-groove region and groove region, respectively. The variables  $\alpha = b_2/(b_1 + b_2)$  and  $\beta$  are the groove width ratio and the groove angle, respectively,  $\omega_0$  and  $\omega_h$  represent the angular speed for the groove part and smooth part, respectively,  $\omega$  is the relative angular speed of the smooth part and the groove part,  $\mu$  is the gas viscosity,  $p_a$  is the ambient pressure, and  $R$  is the bearing radius.

## Appendix B

The dimensionless mass is expressed as follows:

$$\bar{m}_r = m_r \frac{h_{r0}\omega^2}{p_a R^2} \quad (\text{A13})$$

The dimensionless polar rotor inertia and dimensionless transversal rotor inertia can be expressed as:

$$\bar{I}_p = I_p \frac{h_{r0}\omega^2}{p_a R^2 l^2} \quad (\text{A14})$$

$$\bar{I}_T = I_T \frac{h_{r0}\omega^2}{p_a R^2 l^2} \quad (\text{A15})$$

The dimensionless force and moment can be expressed as:

$$\bar{F} = \frac{F}{p_a R^2} \quad (\text{A16})$$

$$\bar{M} = \frac{M}{p_a R^2 l} \quad (\text{A17})$$

Moreover, in Eq. (8),  $\bar{X} = X/h_{r0}$  and  $\bar{Y} = Y/h_{r0}$  represent the dimensionless displacement along  $x$  and  $y$  direction, respectively,  $\bar{\xi} = \xi/h_{r0}$  and  $\bar{\psi} = \psi/l/h_{r0}$  represent the dimensionless rotating angle along  $\xi$  and  $\psi$  direction, respectively, and  $l$  represents the bearing span. The dimensionless time is  $\bar{t} = \omega t$ .

## Appendix C

**Fig. C1** shows the measurement of the groove profile with the roughness meter Rugosurf 90G. The results suggest that the roughness of the groove region is not as low as the one of the ridge region. Therefore, we assume, that the nominal groove depth has a deviation of  $\pm 1 \mu\text{m}$  deviation.

**Fig. C2** shows the measurement of the groove angle with the microscope HiROX KH-8700. The measured groove angle ( $146^\circ$ ) correlates well with the nominal parameter ( $146.2^\circ$ ), which suggests an ignorable deviation.

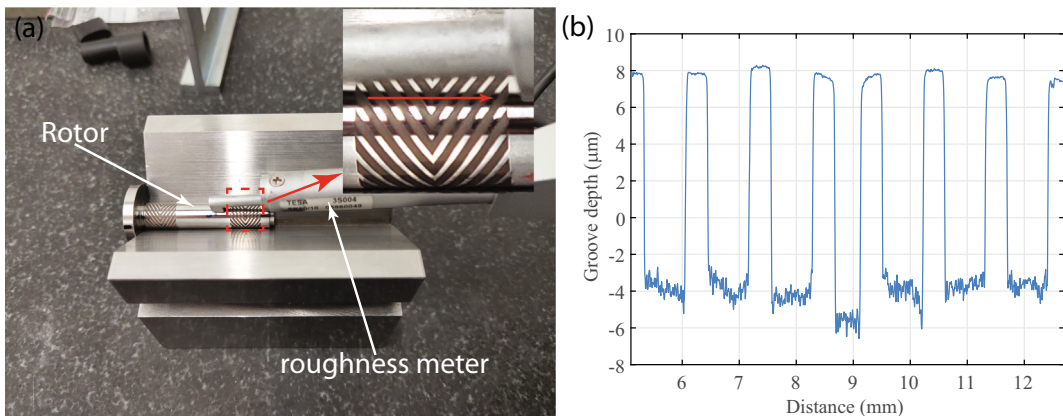


**Fig. C1.** Groove profile measurement: (a) photo of the measurement procedures and (b) the measured groove profile.

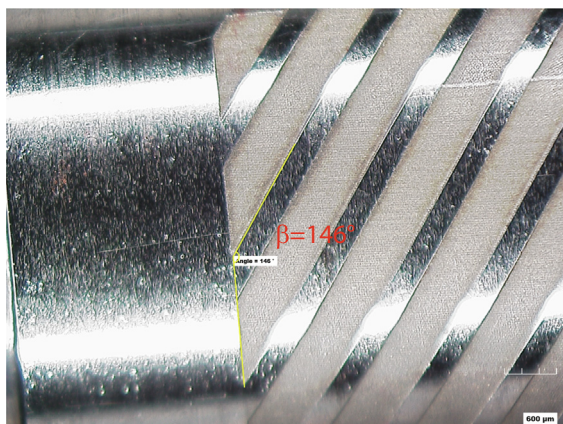


**Fig. C2.** Groove angle measurement result.

## References

- [1] W.G. Denhard, C.H.T. Pan, Application of gas-lubricated bearings to instruments, *J. Lubr. Tech.* 90 (1968) 731–739, <https://doi.org/10.1115/1.3601709>.
- [2] J. Schiffmann, D. Favrat, Experimental investigation of a direct driven radial compressor for domestic heat pumps, *Int. J. Refrig.* 32 (2009) 1918–1928, <https://doi.org/10.1016/j.ijrefrig.2009.07.006>.
- [3] T.H. Kim, Y.-B. Lee, T.Y. Kim, K.H. Jeong, Rotordynamic performance of an oil-free turbo blower focusing on load capacity of gas foil thrust bearings, in: American Society of Mechanical Engineers Digital Collection, 2012, pp. 643–650, <https://doi.org/10.1115/GT2011-46471>.
- [4] J. Zhu, K. Ono, A comparison study on the performance of four types of oil lubricated hydrodynamic thrust bearings for hard disk spindles, *J. Tribol.* 121 (1999) 114–120, <https://doi.org/10.1115/1.2833790>.
- [5] S. Tanaka, S. Togo, H. Kanebako, Development of Micromachine Gas Turbines at Tohoku University, 2005.
- [6] Y.-B. Lee, S. Bum Kwon, T.H. Kim, K. Sim, Feasibility study of an oil-free turbocharger supported on gas foil bearings via on-road tests of a two-liter class diesel vehicle, *J. Eng. Gas Turbines Power* 135 (2013) 052701–052701-10, <https://doi.org/10.1115/1.4007883>.
- [7] G.L. Agrawal, Foil Air/Gas Bearing Technology – An Overview, 1997, V001T04A006, doi: 10.1115/97-GT-347.
- [8] J.W. Powell, A review of progress in gas lubrication, *Rev. Phys. Technol.* 1 (1970) 96–129, <https://doi.org/10.1088/0034-6683/1/2/303>.
- [9] C. Dellacorte, A new foil air bearing test rig for use to 700°C and 70,000 rpm, *Tribol. Trans.* 41 (1998) 335–340, <https://doi.org/10.1080/10402009808983756>.
- [10] M. Diehl, C. Schreiber, J. Schiffmann, The role of Reynolds number effect and tip leakage in compressor geometry scaling at low turbulent Reynolds numbers, *J. Turbomach.* (n.d.) 1–14, doi:10.1115/1.4045465.
- [11] J.H. Vohr, C.Y. Chow, Characteristics of herringbone-grooved, gas-lubricated journal bearings, *J Basic Eng* 87 (1965) 568–576, <https://doi.org/10.1115/1.3650607>.
- [12] C.H. Pan, Spectral Analysis of Gas Bearing Systems for Stability Studies, Mechanical Technology Inc, Latham NY, 1964 (accessed January 23, 2019) <https://apps.dtic.mil/docs/citations/AD0610872>.
- [13] R.E. Cunningham, D.P. Fleming, W.J. Anderson, Experimental load capacity and power loss of herringbone grooved gas lubricated journal bearings, *J. Lubr. Tech.* 93 (1971) 415–422, <https://doi.org/10.1115/1.3451610>.
- [14] R.E. Cunningham, D.P. Fleming, W.J. Anderson, Experimental stability studies of the herringbone-grooved gas-lubricated journal bearing, *J. Lubr. Tech.* 91 (1969) 52–57, <https://doi.org/10.1115/1.3554896>.
- [15] S.B. Malanowski, Experiments on an ultrastable gas journal bearing, *J. Lubr. Tech.* 89 (1967) 433–438, <https://doi.org/10.1115/1.3617021>.
- [16] R.T.P. Whipple, Theory of the Spiral Grooved Thrust Bearing with Liquid or gas lubricant, Great Britain Atomic Energy Research Establishment, Harwell, Berks, England, 1951.
- [17] E.A. Muijderman, Spiral Groove Bearings [Doctor], Technological University Delft, Delft, 1964.

- [18] E.A. Muijderman, Analysis and design of spiral-groove bearings, *J. Lubr. Tech.* 89 (1967) 291–305, <https://doi.org/10.1115/1.3616974>.
- [19] J.H. Vohr, C.H.T. Pan, On the Spiral-Grooved, Self-Acting, Gas Bearing, Mechanical Technology Inc., Latham, N.Y., 1964 (accessed May 8, 2019) <https://www.osti.gov/biblio/4089486-spiral-grooved-self-acting-gas-bearing>.
- [20] N. Miyanaga, J. Tomioka, Stability analysis of herringbone-grooved aerodynamic journal bearings for ultra high-speed rotations, *IJMMM* 4 (2015) 156–161, <https://doi.org/10.7763/IJMMM.2016.V4.246>.
- [21] N. Miyanaga, J. Tomioka, Effect of support stiffness and damping on stability characteristics of herringbone-grooved aerodynamic journal bearings mounted on viscoelastic supports, *Tribol. Int.* 100 (2016) 195–203, <https://doi.org/10.1016/j.triboint.2016.01.019>.
- [22] N. Miyanaga, J. Tomioka, Stability threshold of herringbone-grooved aerodynamic journal bearings with considering frequency dependence of external stiffness and damping elements, *JJSDE* (2016), 2015.2659.
- [23] R.H.M. van der Stegen, Numerical modelling of self-acting gas lubricated bearings with experimental verification, 1997, <https://research.utwente.nl/en/publications/numerical-modelling-of-self-acting-gas-lubricated-bearings-with-e-2> (accessed May 8, 2019).
- [24] V. Castelli, J. Pivrcs, Review of numerical methods in gas bearing film analysis, *J. Lubr. Tech.* 90 (1968) 777–790, <https://doi.org/10.1115/1.3601719>.
- [25] M.M. Reddi, T.Y. Chu, Finite element solution of the steady-state compressible lubrication problem, *J. Lubr. Tech.* 92 (1970) 495–502, <https://doi.org/10.1115/1.3451453>.
- [26] D. Bonneau, J. Absi, Analysis of aerodynamic journal bearings with small number of herringbone grooves by finite element method, *J. Tribol.* 116 (1994) 698–704, <https://doi.org/10.1115/1.2927320>.
- [27] M. Arghir, A. Alsayed, D. Nicolas, The finite volume solution of the Reynolds equation of lubrication with film discontinuities, *Int. J. Mech. Sci.* 44 (2002) 2119–2132, [https://doi.org/10.1016/S0020-7403\(02\)00166-2](https://doi.org/10.1016/S0020-7403(02)00166-2).
- [28] B.A. Miller, I. Green, Numerical formulation for the dynamic analysis of spiral-grooved gas face seals, *J. Tribol.* 123 (2001) 395–403, <https://doi.org/10.1115/1.1308015>.
- [29] M. Arghir, S.L. Lez, J. Frene, Finite-volume solution of the compressible Reynolds equation: Linear and non-linear analysis of gas bearings, *Proc. Inst. Mech. Eng., Part J: J. Eng. Tribol.* 220 (2006) 617–627, <https://doi.org/10.1243/13506501JET161>.
- [30] M.T.C. de Faria, *Finite Element Analysis of High-speed Grooved Gas Bearings*, Texas A & M University, 1999.
- [31] J. Schiffmann, D. Favrat, Integrated design and optimization of gas bearing supported rotors, *J. Mech. Des.* 132 (2010) 051007–051007-11, <https://doi.org/10.1115/1.4001381>.
- [32] E. Guenat, J. Schiffmann, Real-gas effects on aerodynamic bearings, *Tribol. Int.* 120 (2018) 358–368, <https://doi.org/10.1016/j.triboint.2018.01.008>.
- [33] G.H. Jang, J.W. Yoon, Nonlinear dynamic analysis of a hydrodynamic journal bearing considering the effect of a rotating or stationary herringbone groove, *J. Tribol.* 124 (2002) 297–304, <https://doi.org/10.1115/1.1401019>.
- [34] G.G. Hirs, The load capacity and stability characteristics of hydrodynamic grooved journal bearings, *ASLE Trans.* 8 (1965) 296–305, <https://doi.org/10.1080/05698196508972102>.
- [35] C.-C. Wang, Bifurcation analysis of an aerodynamic journal bearing system considering the effect of stationary herringbone grooves, *Chaos Solitons Fract.* 33 (2007) 1532–1545, <https://doi.org/10.1016/j.chaos.2006.03.011>.
- [36] C.-C. Wang, Theoretical and nonlinear behavior analysis of a flexible rotor supported by a relative short herringbone-grooved gas journal-bearing system, *Physica D: Nonlinear Phenom.* 237 (2008) 2282–2295, <https://doi.org/10.1016/j.physd.2008.02.004>.
- [37] J.S. Larsen, I.F. Santos, On the nonlinear steady-state response of rigid rotors supported by air foil bearings—theory and experiments, *J. Sound Vib.* 346 (2015) 284–297, <https://doi.org/10.1016/j.jsv.2015.02.017>.
- [38] P. Bonello, H.M. Pham, The efficient computation of the nonlinear dynamic response of a foil–air bearing rotor system, *J. Sound Vib.* 333 (2014) 3459–3478.
- [39] B. Bou-Saïd, G. Grau, I. Jordanoff, On nonlinear rotor dynamic effects of aerodynamic bearings with simple flexible rotors, *J. Eng. Gas Turbines Power* 130 (2008), <https://doi.org/10.1115/1.2747262>.
- [40] D. Kim, Parametric studies on static and dynamic performance of air foil bearings with different top foil geometries and bump stiffness distributions, *J. Tribol.* 129 (2007) 354–364, <https://doi.org/10.1115/1.2540065>.
- [41] K. Feng, W. Liu, X. Zhao, W. Li, Nonlinear numerical prediction of a rotor-bearing system using damped flexure pivot tilting pad gas bearings, *Tribol. Trans.* 60 (2017) 448–459, <https://doi.org/10.1080/10402004.2016.1177151>.
- [42] J.S. Larsen, I.F. Santos, S.V. Osmanski, Stability of rigid rotors supported by air foil bearings: comparison of two fundamental approaches, *J. Sound Vib.* 381 (2016) 179–191.
- [43] L. Gu, E. Guenat, J. Schiffmann, A review of grooved dynamic gas bearings, *Appl. Mech. Rev.* 72 (2020), <https://doi.org/10.1115/1.4044191>.
- [44] S.P. Timoshenko, J.N. Goodier, *Theory of Elasticity*, McGraw-Hill, New York, 1970.
- [45] D. Kim, Parametric studies on static and dynamic performance of air foil bearings with different top foil geometries and bump stiffness distributions, *J. Tribol.* 129 (2006) 354–364, <https://doi.org/10.1115/1.2540065>.
- [46] P. Bonello, H.M. Pham, Nonlinear dynamic analysis of high speed oil-free turbomachinery with focus on stability and self-excited vibration, *J. Tribol.* 136 (2014) 216–223.
- [47] L. Shampine, M. Reichelt, The MATLAB ODE suite, *SIAM J. Sci. Comput.* 18 (1997) 1–22, <https://doi.org/10.1137/S1064827594276424>.
- [48] P.H. Wagner, Z. Wuillemin, S. Diethelm, J. Van herle, J. Schiffmann, Modeling and designing of a radial anode off-gas recirculation fan for solid oxide fuel cell systems, *J. Electrochem. En. Conv. Stor.* 14 (2017), <https://doi.org/10.1115/1.4036401>.
- [49] P.H. Wagner, J. Van herle, J. Schiffmann, Theoretical and experimental investigation of a small-scale, high-speed, and oil-free radial anode off-gas recirculation fan for solid oxide fuel cell systems, *J. Eng. Gas Turbines Power* 142 (2020), <https://doi.org/10.1115/1.4045104>.
- [50] P.H. Wagner, Z. Wuillemin, D. Constantin, S. Diethelm, J. Van herle, J. Schiffmann, Experimental characterization of a solid oxide fuel cell coupled to a steam-driven micro anode off-gas recirculation fan, *Appl. Energy* 262 (2020) 114219, <https://doi.org/10.1016/j.apenergy.2019.114219>.
- [51] E. Guenat, J. Schiffmann, Multi-objective optimization of grooved gas journal bearings for robustness in manufacturing tolerances, *Tribol. Trans.* 62 (2019) 1041–1050, <https://doi.org/10.1080/10402004.2019.1642547>.
- [52] E. Guenat, J. Schiffmann, Dynamic force coefficients identification on air-lubricated herringbone grooved journal bearing, *Mech. Syst. Signal Process.* 136 (2020) 106498, <https://doi.org/10.1016/j.ymssp.2019.106498>.
- [53] E. Iseli, E. Guenat, R. Tresch, J. Schiffmann, Analysis of spiral-grooved gas journal bearings by the narrow-groove theory and the finite element method at large eccentricities, *J. Tribol.* 142 (2020), <https://doi.org/10.1115/1.4045636>.
- [54] W.J. Chen, *Practical Rotordynamics and Fluid Film Bearing Design*, Eigen Technologies, Incorporated, 2015.